

Communication

Co-Based Nanosheets with Transitional Metal Doping for Oxygen Evolution Reaction

Chunhua Xiong ¹  and Chao Cai ^{2,*}

¹ College of Air Traffic Management, Civil Aviation Flight University of China, Guanghan 618307, China; xch@cafuc.edu.cn

² School of Physics, University of Electronic Science and Technology of China, Chengdu 610054, China

* Correspondence: zchaotsai@163.com

Abstract: Activated two-dimension (2D) materials are used in various applications as high-performance catalysts. Breaking the long-range order of the basal plane of 2D materials can highly promote catalytic activity by supplying more active sites. Here we developed a method to synthesize ultrathin MCoO_x (M = V, Mn, Fe, Ni, Cu, Zn) amorphous nanosheets (ANSs). These Co-based ANSs show high oxygen evolution reaction (OER) activity in alkaline solution due to the broken long-range order and the presence of abundant low bonded O on the basal plane. The stable Fe₁Co₁O_x ANSs also show an overpotential of ca. 240 mV of achieving 10 mA/cm² in OER, better than most reported transition metal-based electrocatalysts.

Keywords: transition metal-based materials; two-dimension nanosheets; amorphous materials; electrocatalysts; low bonded oxygen



Citation: Xiong, C.; Cai, C. Co-Based Nanosheets with Transitional Metal Doping for Oxygen Evolution Reaction. *Nanomaterials* **2022**, *12*, 1788. <https://doi.org/10.3390/nano12111788>

Academic Editors: Yuichi Negishi, Vincenzo Vaiano, Olga Sacco and Gianvito Vilé

Received: 19 March 2022

Accepted: 20 May 2022

Published: 24 May 2022

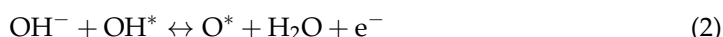
Publisher's Note: MDPI stays neutral with regard to jurisdictional claims in published maps and institutional affiliations.



Copyright: © 2022 by the authors. Licensee MDPI, Basel, Switzerland. This article is an open access article distributed under the terms and conditions of the Creative Commons Attribution (CC BY) license (<https://creativecommons.org/licenses/by/4.0/>).

1. Introduction

As a fundamental electrochemical half-reaction, oxygen evolution reaction (OER) is involved in various important energy-related technological applications, such as water splitting [1] and Zn-air batteries [2]. However, the sluggish dynamic of the four electron process in OER has highly hindered the development of the oxygen-involved reaction. The relevant reaction process is shown below [3].

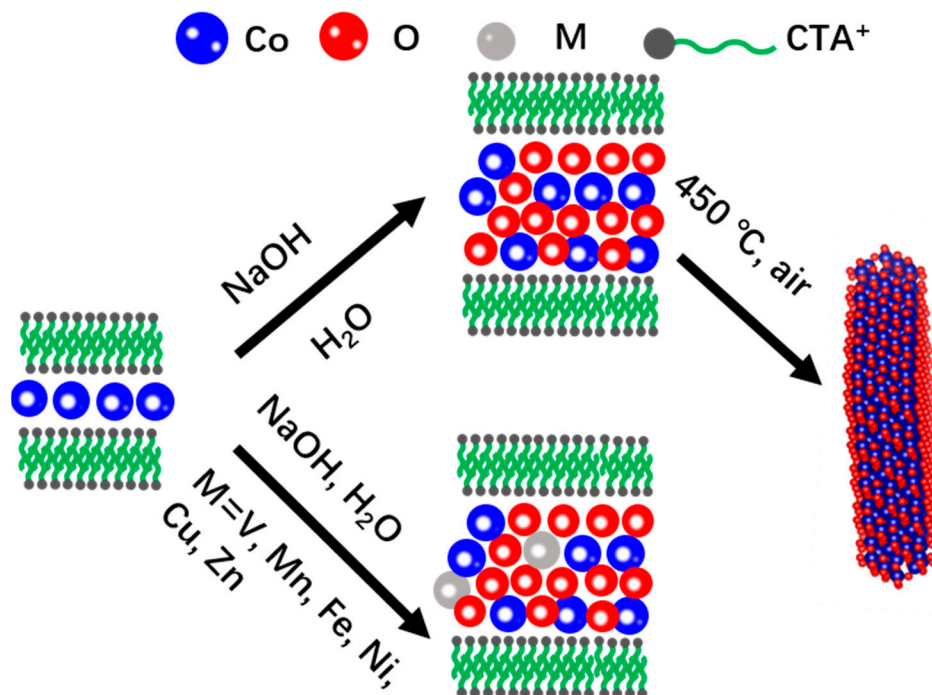


Currently demonstrated electrocatalysts for OER are Ru/Ir-based materials [4], which are costly to realize the practical applications. Developing low-cost, efficient electrocatalysts is a potential approach to meet the demand of various applications [5,6]. Transition metal-based catalysts are widely investigated for OER, including oxides [5], phosphides [7], selenides [8], etc. Co-based nanostructures show high catalytic activity and stability in OER, demonstrated by numerous investigations [9–11]. Unfortunately, these emerging catalysts still suffer insufficient development, especially in those novel and facile approaches for preparing desired electrocatalysts of such materials with well-defined nanostructures. Therefore, exploring new methods for synthesizing uniform nanomaterials is significant for a wide range of applications and for developing modern synthetic methodology.

Two-dimension (2D) materials are widely used as electrocatalysts because of their high surface area for contacting electrolytes [12], the low energy barrier for mediums absorption [13], and the Fermi-level nearby density of states that resemble noble metals [14].

However, the active sites for catalytic applications are usually located at the edge and defective sites, such as MoS₂ [15], WS₂ [16], WSe₂ [17], etc. Therefore, the basal plane activation is a primary issue in generating efficient catalysts based on 2D materials. The current methods to activate the basal plane are localized area modification, such as manufacturing defects [15], introducing alien species [18], and partially oxidizing atoms on the basal plane [19]. However, realizing large area activation on 2D materials still is a challenge to obtain desired catalysts. Breaking the long-range order can be an efficient way to generate more active sites or realize the large area activation on 2D materials [20]. For instance, the amorphous FeCo-hydroxide nanosheets (NSs) can obtain more active sites by modifying the OH[−] on the basal plane [21]. Meanwhile, breaking the long-range order of FePO₄ also can achieve better OER activity than the crystallized one [22]. Moreover, this activation method also can be used to manipulate the crystal/amorphous feature of FeCoPO₄ to obtain a higher activity of hydrogen evolution reaction [23]. Therefore, exploring the general approach to synthesizing amorphous 2D materials could be an emerging point for developing efficient catalysts.

Co-based materials are widely used for OER due to their high intrinsic activity, processability at the atomic scale, and low-cost [24,25]. Albeit many strategies have been developed to generate Co-based materials, the common methods cannot generate amorphous nanosheets, such as the hydrothermal method, [26] sol–gel method [27], chemical vapor method [28], etc. In this work, we synthesized various Co-based amorphous nanosheets (ANSs) using the coprecipitation method in a cetyltrimethylammonium bromide (CTAB) solution. We demonstrate the sheet-like morphology of Co-based materials is remained after introducing alien species, including V, Mn, Fe, Ni, Cu, and Zn oxides (Scheme 1). The thickness of CoO_x and Fe₁Co₁O_x ANSs is only ca. 1 nm. This method can also be used to synthesize ultrathin NiO_x ANSs. The Fe doping in CoO_x NSs leads to the oxidation process of Co³⁺ to Co⁴⁺ in OER. CoO_x ANSs show higher OER activity than the crystallized Co₃O₄ NSs, demonstrating that low bonded oxygen can also promote the OER. CoO-based materials show high activity in OER, with the overpotential of ca. 240 mV for achieving 10 mA/cm² (Fe₁Co₁O_x ANSs).



Scheme 1. The growth process of CoO-based ANSs. This method also can be used to synthesize NiO ANSs with Ni substituted Co in the first step.

2. Materials and Methods

We concluded the growth process of CoO-based ANSs, as shown in Scheme 1. Details of synthesis procedure can be found in supporting materials. The Powder X-ray diffraction (XRD) pattern shows the amorphous feature of CoO_x ANSs (Figure S1). MCoO_x (M = V, Mn, Fe, Ni, Cu, and Zn) ANSs are synthesized by using M/Co molar ratios of 1:1. The amorphous feature remains after doping Fe, being verified by XRD (Figure S1). The Fe, Co, and O show homogeneous distribution being demonstrated by the energy dispersive spectroscopy (EDS) method (Figure S2). The 2D morphologies of MCoO_x ANSs are checked by scanning electron microscopy (SEM) (Figure S3). For comparison, crystallized Co₃O₄ NSs are prepared by annealing CoO_x ANSs. Peaks in XRD pattern of Co₃O₄ NSs are consistent with JCPDS No. 43-1003 (Figure S4).

3. Results

3.1. Electrochemical Performance

The catalytic activity of various Co-based ANSs is tested in a polytetrafluoroethylene (PTFE) bottle. We used Co-based ANSs as electrocatalysts for OER in 1 M KOH at room temperature (current density in this work is normalized by the geometric area of the used electrode). To begin with, we demonstrated that CoO_x ANSs show better OER performance than Co₃O₄ NSs (Figure S5). This result indicates that breaking the long-range order on 2D materials can activate the basal plane for catalytic activity [20]. The electrochemical surface area (ECSA) value is positively related to the number of active sites. The CoO_x ANSs possess an ECSA of 4-fold of Co₃O₄ NSs (Figure S6), demonstrating the highly increased active site numbers in CoO_x ANSs. Figure 1a plots the polarization curves of Co-based ANSs. These MCoO_x ANSs show better OER activity than commercial IrO₂, comparing the overpotential of achieving a current density of 10 mA/cm² (Table S1). Small Tafel slope benefits the practical applications, where the highly increased current density needs only a low potential increase. The Fe₁Co₁O_x ANSs show the lowest Tafel slope (ca. 50 mV/dec) value among those prepared MCoO_x ANSs (Figure 1b) (Table S1). Figure 1c summarizes the overpotential of achieving 10 mA/cm² of MCoO_x ANSs and commercial IrO₂. Fe₁Co₁O_x ANSs possess an overpotential of ca. 240 mV, which is better than other MCoO_x ANSs (Table S1) and the state-of-art Co-based OER catalysts (Table S2) [29–40]. The higher mass activity shows the lower cost of OER catalysts in practical applications. As shown in Figure 1d, The Fe₁Co₁O_x ANSs show the highest mass activity of ca. 353 A/g, which is ca. 19-fold of commercial IrO₂ (ca. 18.53 A/g). Fe₁Co₁O_x ANSs also show good activity and structural stability in OER at 1.5 V vs. RHE (Figure S7). Compared to the stability test of Co-based NSs (Figure S5), we concluded that Co could be responsible for the high stability of OER activity. Indeed, these results demonstrate the highly promising Fe₁Co₁O_x ANSs as practical catalysts for OER.

3.2. Structural Characterization

The structural characterizations focus on the Fe₁Co₁O_x ANSs because Fe₁Co₁O_x ANSs show the best OER activity (Figure 1). As shown in Figure 2, we use SEM and transmission electron microscopy (TEM) method to character ANSs. SEM and TEM images show that CoO_x ANSs have well-defined 2D structures (Figure 2a,b). The selected area electron diffraction (SAED) pattern, inset in Figure 2b, certifies the amorphous feature of CoO_x ANSs again. Figure 2b shows that CoO_x ANSs possess a thickness of ca. 1 nm. The SEM and low magnification high angle annular dark field (HAADF) images (Figure 2c,d) show the hierarchical nanostructure of Fe₁Co₁O_x ANSs, with a width of ca. 400 nm. A high-resolution HAADF image verifies the Fe₁Co₁O_x ANSs thickness of ca. 1 nm, as shown in Figure 2e. EDS mapping shows the homogeneous distribution of Fe, Co, and O (Figure 2f). The ultrathin Co-based ANSs formation can be attributed to the surfactant of CTAB (with a high concentration of 0.05 M) and NaOH (with fast precipitation rate in solution, formation of amorphous MCoO_x ANSs) [41]. The concentration of CTAB is above 2-fold its second micelle concentration (0.021 M) [42], leading to the CTAB micelles in reaction solution tending to form two layer structures (Scheme 1). The ultrathin layer

structure and elemental homogeneous distribution of $\text{Fe}_1\text{Co}_1\text{O}_x$ ANSs may be caused by the fast nuclei of Fe and Co in alkaline solution during the coprecipitation process. This growth mechanism also works in synthesizing NiO_x ANSs (Figures S8 and S9).

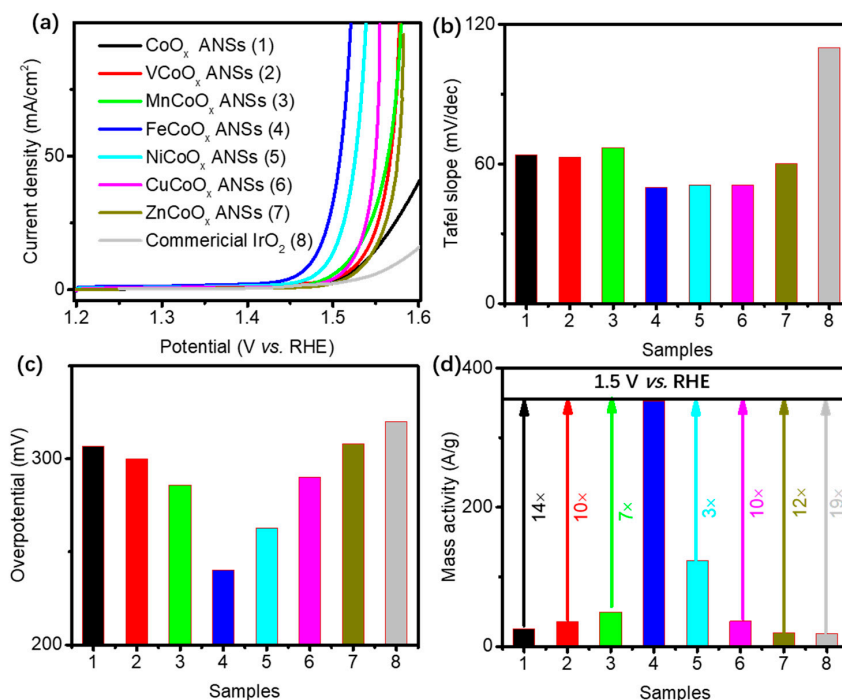


Figure 1. Electrochemical characterization of MCoO_x ANSs. Polarization curves (a), specific Tafel slopes (b), specific overpotential of achieving 10 mA/cm^2 (c), and specific mass activity at 1.5 V vs. RHE (d) of Co-based ANSs. $\text{Fe}_1\text{Co}_1\text{O}_x$ ANSs show highest OER activity among these Co-based ANSs.

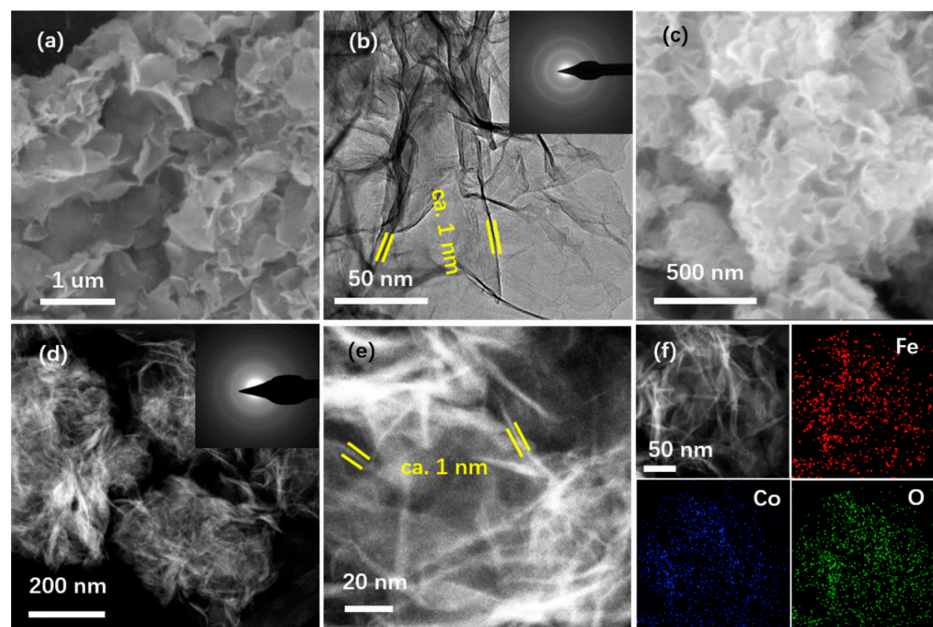


Figure 2. Structural characterization of CoO_x ANSs and $\text{Fe}_1\text{Co}_1\text{O}_x$ ANSs. SEM image (a) and TEM image of CoO_x ANSs (b). Inset in (b) is SAED pattern of CoO_x ANSs. SEM image (c), low magnification HAADF image (d), high magnification image (e), EDS mapping (f) of $\text{Fe}_1\text{Co}_1\text{O}_x$ ANSs. Inset in (d) is SAED pattern of $\text{Fe}_1\text{Co}_1\text{O}_x$ ANSs. The CoO ANSs and $\text{Fe}_1\text{Co}_1\text{O}_x$ ANSs possess similar thickness of ca. 1 nm.

4. Discussion

4.1. Surface Chemistry

The strong synergistic effect between cation and anion in FeCo-based nanocrystals is usually used to generate highly active OER electrocatalysts [43,44]. Herein, X-ray photoelectron spectrum (XPS) is used to check the electronic configuration and O state of CoO_x ANSs and $\text{Fe}_1\text{Co}_1\text{O}_x$ ANSs. Figure 3a shows the survey spectrum of CoO_x ANSs and $\text{Fe}_1\text{Co}_1\text{O}_x$ ANSs. Figure 3b plots the fitted O 1s spectrum. The three characteristic peaks of O 1s are consistent with oxygen atoms bound to metal atoms (530.9 eV), low bonded oxygen (531.8 eV), OH^- or surface-adsorbed oxygen (532.7 eV), and water molecules on the surface (533.74 eV) [45]. The CoO_x ANSs have a low bonded oxygen ratio of 49.4%, higher than 18.0% of Co_3O_4 NSs (Figure S10), demonstrating that the broken long-range order of ANSs leads to a high ratio of O in NSs. Moreover, extra Fe doping leads to the larger low bonded O ratio of 45.5% in $\text{Fe}_1\text{Co}_1\text{O}_x$ ANSs, because Fe can modify the adsorption state of surrounded Co. To clarify this, we analyze the state variations of Co after Fe doping. Figure 3c summarizes the fitted Co 2p spectrum of CoO_x ANSs and $\text{Fe}_1\text{Co}_1\text{O}_x$ ANSs. The peaks located at ca. 796.7 eV and ca. 780.9 eV correspond to $\text{Co } 2p_{1/2}$ and $\text{Co } 2p_{3/2}$ of Co^{3+} , respectively [29]. The peaks of Co^{2+} appear at ca. 781.1 eV (CoO_x ANSs) to ca. 781.8 eV ($\text{Fe}_1\text{Co}_1\text{O}_x$ ANSs). The $\text{Co}^{2+}/\text{Co}^{3+}$ ratio in $\text{Fe}_1\text{Co}_1\text{O}_x$ ANSs (0.61) is higher than 0.55 in CoO_x ANSs. The high Co^{2+} ratio in $\text{Fe}_1\text{Co}_1\text{O}_x$ ANSs can be due to the extra Fe bonds on some O near the Co center. Figure 3d shows the fitted Fe 2p spectrum. The peaks located at ca. 720.5 eV and ca. 707.7 eV are consistent with $2p_{1/2}$ and $2p_{3/2}$ of Fe^{3+} , respectively [46]. Therefore, the Co modulation is determined by the Fe^{3+} , leading to the OER activity increase.

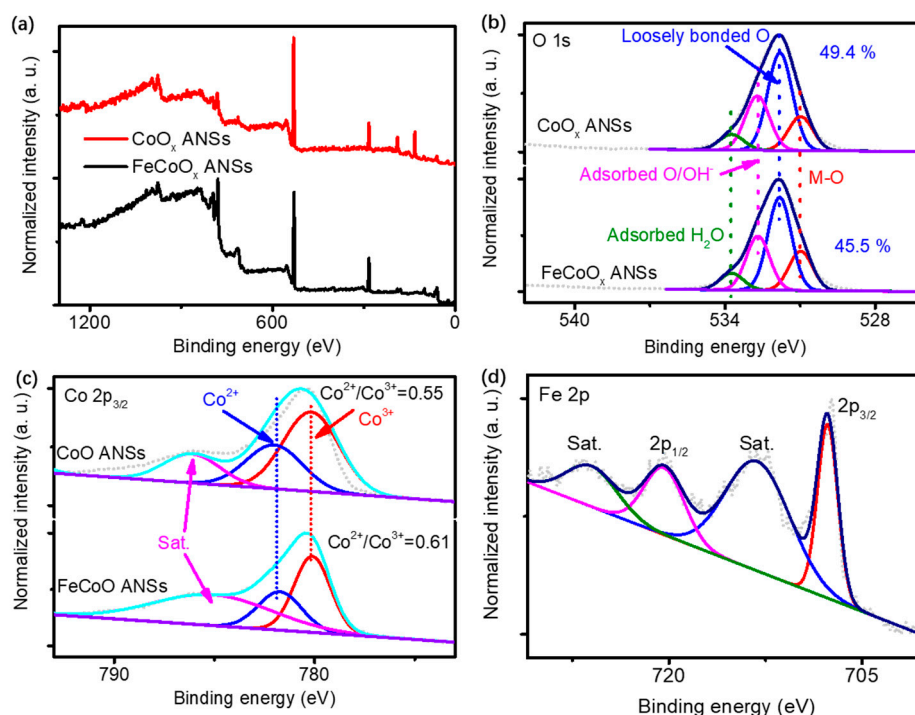


Figure 3. XPS spectrum of CoO_x ANSs and $\text{Fe}_1\text{Co}_1\text{O}_x$ ANSs. Survey spectrum (a), O 1s spectrum (b), Co 2p spectrum of CoO_x ANSs and FeCoO_x ANSs (c), and Fe 2p spectrum of FeCoO_x ANSs (d). The Fe loading on CoO_x ANSs makes the change of Co 2p peaks, verifying the strong synergistic effect between Fe and Co oxides in 2D structures.

4.2. Reaction Process

The high valance Co ions are considered the active sites for OER at a high potential of 1.24 to 1.54 V vs. RHE (Co^{3+} and Co^{4+}) [47]. The intrinsic activity of Co-based materials is usually determined by the Co^{3+} and Co^{4+} formation during OER. The abundant low

bonded oxygen can promote the high Co cations formation; Refs. [48,49] meanwhile lead to the formation of delocalized electrons in Co, and thus promote the adsorption efficiency of water molecules on Co cations and enhance conductivity and catalytic activity [50–52]. Furthermore, the low bonded O in CoO_x ANSs can be regarded as pre-activated O^{2-} or O^0 , which can be preferentially oxidized or released during OER and thus promote the OER [53]. These appearances are demonstrated by the fact that low bonded O-rich CoO_x ANSs have higher OER activity than Co_3O_4 NSs (Figures S5 and S6). Moreover, the Fe can promote the OER activity of Co by decreasing the intermediate formation energy [54], the adsorption energy of OH^- , and the desorption efficiency of O during OER [55]. This feature can lead to an ECSA value increase [46]. Figure 4a shows that $\text{Fe}_1\text{Co}_1\text{O}_x$ ANSs possess the ECSA value of ca. 75.1 mF/cm^2 , which is 2-fold of CoO_x ANSs (ca. 31.8 mF/cm^2). Moreover, the changed electronic state on Co also can promote the conductivity, which shows an impact on efficacious charge transfer between support and catalysts [1,48]. The charge transfer resistance (R_{ct}) is analyzed by electrochemical impedance spectrum (EIS) (measured at 1.53 V vs. RHE), as shown in Figure 4b. The R_{ct} of $\text{Fe}_1\text{Co}_1\text{O}_x$ ANSs is ca. 9.6Ω , which is smaller than 39.7Ω of CoO_x ANSs, suggesting an accelerated charge transfer coefficient between FeCoO_x ANSs and support. Indeed, the outstanding OER activity of FeCoO_x ANSs may originate from the abundant low bonded O, intrinsic activity of Co, which is highly activated by Fe^{3+} .

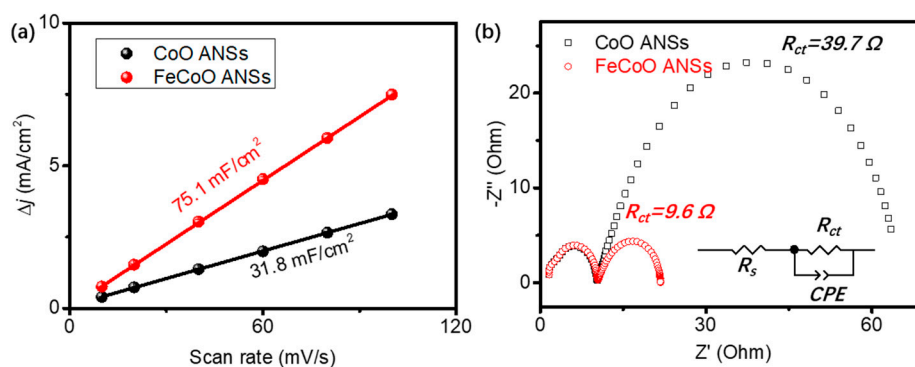


Figure 4. Analysis of catalysts and electrode. ECSA (a) and Nyquist plots (b) of ANS. The Fe doping can effectively promote the reactive sites with ca. 2-fold (a). The charge transfer efficiency between glassy carbon support and FeCoO_x ANSs is very low (b). ECSA is calculated from double layered capacitance (C_{dl}) at 1.15 V vs. RHE.

4.3. Fe Doping Amount

As the above results show, Fe plays an important role in determining the OER activity of $\text{Fe}_x\text{Co}_{1-x}\text{O}_y$ ANSs. The OER activity is amount doping dependent in synergistic hybrids. The $\text{Fe}_x\text{Co}_{1-x}\text{O}_y$ ANSs with different Fe atom doping show similar onset potential in OER (around 1.42 V vs. RHE) (Figure S11), far lower than the one of 1.49 V vs. RHE in CoO_x ANSs (70 mV). Moreover, Figure S5a shows that the onset potential of Co_3O_4 NSs is 1.52 V vs. RHE, lower than the one in CoO_x ANSs (30 mV). These results indicate that the OER rate and characteristic activity are major determined by the Fe but not the low bonded oxygen in $\text{Fe}_1\text{Co}_1\text{O}_x$ ANSs. After Fe doping, the adsorption energy state of these negatively charged species on the $\text{Co}^{3+}/\text{Co}^{4+}$ delocalized center can be different, which is sensitive to the difference in the electron affinity between Fe (15 kJ/mol) and Co (63 kJ/mol) [48]. The high electron affinity of Co ensures the high concentration of negatively charged species around Co cations with low bonded or activated O surrounded, with accelerated $\text{Co}^{3+}/\text{Co}^{4+}$ formation during OER [49]. The concentrated negatively charged species around Co in $\text{Fe}_x\text{Co}_{1-x}\text{O}_y$ ANSs also relates to the Fe doping ratio in the ANS's system [6,56–59]. $\text{Fe}_x\text{Co}_{1-x}\text{O}_y$ ANSs with different Fe molar ratio doping show modified charge transport efficiency (Figure S11b). $\text{Fe}_1\text{Co}_1\text{O}_x$ ANSs show the lowest Tafel slope of 50 mV/dec, verifying the highest adsorption/desorption efficiency on delocalized Co cations center with low bonded or activated O surrounded in OER. By further increasing

the Fe doping to 0.8 mmol, the Tafel slope increases (67 mV/dec) because Fe oxides itself is not good OER catalysts. Therefore, optimization of Fe doping in $\text{Fe}_1\text{Co}_1\text{O}_x$ ANSs determines the OER activity by changing the absorption/desorption on $\text{Co}^{3+}/\text{Co}^{4+}$ cations surrounded by low bonded O and activated O.

5. Conclusions

In conclusion, we developed a general approach for preparing ultrathin Co-based ANSs with abundant low bonded oxygen. The intrinsic OER activity of Co-based ANSs can be modified by introducing alien species, where the Fe doped Co NSs possess the highest OER activity. Such superior OER activity of $\text{Fe}_1\text{Co}_1\text{O}_x$ ANSs benefits from the promoted oxidation process of Co^{3+} to Co^{4+} , high intrinsic catalytic activity, and large electrochemically active surface area. We believe that this work developed a potential way to generate highly efficient catalysts based on activated 2D materials.

Supplementary Materials: The following supporting information can be downloaded at: <https://www.mdpi.com/article/10.3390/nano12111788/s1>, Figure S1: XRD pattern of as-prepared CoO_x and $\text{Fe}_1\text{Co}_1\text{O}_x$ NSs; Figure S2: EDS mapping of $\text{Fe}_1\text{Co}_1\text{O}_x$ ANSs in SEM modes; Figure S3: SEM images of MCoO_x NSs. These NSs are based on Co, with M: Co molar ratio of 1:1 in solution; Figure S4: XRD pattern and SEM image of Co_3O_4 NSs. Because of the thermal relaxation, the annealed Co_3O_4 NSs shows good crystalline. SEM image clarifies the 2D feature of Co_3O_4 NSs (Figure S4b); Figure S5: Electrochemical characterization of CoO_x ANSs and Co_3O_4 NSs. Polarization curves (a), Tafel slopes (b), stability test of CoO ANSs (c), and stability test of Co_3O_4 NSs (d); Figure S6: ECSA of CoO_x ANSs and Co_3O_4 NSs. C_{dl} is tested from 1.15 V vs. RHE; Figure S7: Accelerating degradation of $\text{Fe}_1\text{Co}_1\text{O}_x$ ANSs in OER. Stability test of $\text{Fe}_1\text{Co}_1\text{O}_x$ ANSs (a) and structure of FeCoO_x ANSs after use (b) in alkaline solution. The collective electron transport (a) and sustained 2D feature (b) in OER demonstrate the high stability of FeCoO_x ANSs for adapting long-time oxidizing condition; Figure S8: SAED and TEM images of NiO_x ANSs. The NiO_x ANSs also show ultrathin 2D feature. In contrast, the width of NiO_x ANSs (ca. 200 nm) is much smaller than CoO_x ANSs (>1 μm); Figure S9: EELS of NiO_x ANSs. The EELS spectrum demonstrates that the Ni-based NSs prepared in CTAB solution is composited by Ni and O; Figure S10: XPS spectrum of Co 2p and O1s of Co_3O_4 NSs; Figure S11: Electrochemical test of $\text{Fe}_x\text{Co}_{1-x}\text{O}_y$ ANSs with different Fe feeding in preparing step. The Co feed amount in these materials is 0.4 mmol; Table S1: Parameter of electrocatalysts for OER in 1 M KOH; Table S2: Collection of reported Co-based electrocatalysts on glassy carbon electrode for OER in 1 M KOH. References [29–40] are cited in the supplementary materials.

Author Contributions: Conceptualization, C.X.; methodology, C.C.; writing—original draft preparation, C.C.; writing—review and editing, C.X.; funding acquisition, C.X. All authors have read and agreed to the published version of the manuscript.

Funding: This work was supported by the National Natural Science Foundation of China under Grant No. 31470822 and 61703292, and by the Fundamental Research Funds for the Central Universities under No. J2021-078.

Institutional Review Board Statement: Not applicable.

Informed Consent Statement: Not applicable.

Data Availability Statement: Not applicable.

Conflicts of Interest: The authors declare no conflict of interest.

References

1. Hu, E.; Feng, Y.; Nai, J.; Zhao, D.; Hu, Y.; Lou, X.W. Construction of hierarchical Ni–Co–P hollow nanobricks with oriented nanosheets for efficient overall water splitting. *Energy Environ. Sci.* **2018**, *11*, 872–880. [CrossRef]
2. Yin, J.; Li, Y.; Lv, F.; Lu, M.; Sun, K.; Wang, W.; Wang, L.; Cheng, F.; Li, Y.; Xi, P.; et al. Oxygen vacancies dominated $\text{NiS}_2/\text{CoS}_2$ interface porous nanowires for portable Zn-air batteries driven water splitting devices. *Adv. Mater.* **2017**, *29*, 1704681. [CrossRef] [PubMed]

3. Sultan, S.; Tiwari, J.N.; Singh, A.N.; Zhumagali, S.; Ha, M.; Myung, C.W.; Thangavel, P.; Kim, K.S. Single atoms and clusters based nanomaterials for hydrogen evolution, oxygen evolution reactions, and full water splitting. *Adv. Energy Mater.* **2019**, *9*, 1900624. [[CrossRef](#)]
4. Seitz, L.C.; Dickens, C.F.; Nishio, K.; Hikita, Y.; Montoya, J.; Doyle, A.; Kirk, C.; Vojvodic, A.; Hwang, H.Y.; Norskov, J.K.; et al. A highly active and stable IrOx/SrIrO₃ catalyst for the oxygen evolution reaction. *Science* **2016**, *353*, 1011–1014. [[CrossRef](#)] [[PubMed](#)]
5. Hwang, J.; Rao, R.R.; Giordano, L.; Katayama, Y.; Yu, Y.; Shao-Horn, Y. Perovskites in catalysis and electrocatalysis. *Science* **2017**, *358*, 751–756. [[CrossRef](#)]
6. Zhang, B.; Zheng, X.; Voznyy, O.; Comin, R.; Bajdich, M.; Garcia-Melchor, M.; Han, L.; Xu, J.; Liu, M.; Zheng, L.; et al. Homogeneously dispersed multimetal oxygen-evolving catalysts. *Science* **2016**, *352*, 333–337. [[CrossRef](#)]
7. Stern, L.-A.; Feng, L.; Song, F.; Hu, X. Ni₂P as a Janus catalyst for water splitting: The oxygen evolution activity of Ni₂P nanoparticles. *Energy Environ. Sci.* **2015**, *8*, 2347–2351. [[CrossRef](#)]
8. Nai, J.; Lu, Y.; Yu, L.; Wang, X.; Lou, X.W. Formation of Ni-Fe mixed diselenide nanocages as a superior oxygen evolution electrocatalyst. *Adv. Mater.* **2017**, *29*, 3870. [[CrossRef](#)]
9. Han, L.; Yu, X.Y.; Lou, X.W. Formation of prussian-blue-analog nanocages via a direct etching method and their conversion into ni-co-mixed oxide for enhanced oxygen evolution. *Adv. Mater.* **2016**, *28*, 4601–4605. [[CrossRef](#)]
10. Lin, Y.; Yang, L.; Zhang, Y.; Jiang, H.; Xiao, Z.; Wu, C.; Zhang, G.; Jiang, J.; Song, L. Defective carbon-CoP nanoparticles hybrids with interfacial charges polarization for efficient bifunctional oxygen electrocatalysis. *Adv. Energy Mater.* **2018**, *8*, 1703623. [[CrossRef](#)]
11. Cai, P.; Huang, J.; Chen, J.; Wen, Z. Oxygen-containing amorphous cobalt sulfide porous nanocubes as high-activity electrocatalysts for the oxygen evolution reaction in an alkaline/neutral medium. *Angew. Chem.* **2017**, *56*, 4858–4861. [[CrossRef](#)] [[PubMed](#)]
12. Yin, J.; Fan, Q.; Li, Y.; Cheng, F.; Zhou, P.; Xi, P.; Sun, S. Ni-C-N nanosheets as catalyst for hydrogen evolution reaction. *J. Am. Chem. Soc.* **2016**, *138*, 14546–14549. [[CrossRef](#)] [[PubMed](#)]
13. Ma, R.; Zhou, Y.; Chen, Y.; Li, P.; Liu, Q.; Wang, J. Ultrafine molybdenum carbide nanoparticles composited with carbon as a highly active hydrogen-evolution electrocatalyst. *Angew. Chem.* **2015**, *54*, 14723–14727. [[CrossRef](#)]
14. Dong, S.; Chen, X.; Zhang, X.; Cui, G. Nanostructured transition metal nitrides for energy storage and fuel cells. *Coord. Chem. Rev.* **2013**, *257*, 1946–1956. [[CrossRef](#)]
15. Lukowski, M.A.; Daniel, A.S.; Meng, F.; Forticaux, A.; Li, L.; Jin, S. Enhanced hydrogen evolution catalysis from chemically exfoliated metallic MoS₂ nanosheets. *J. Am. Chem. Soc.* **2013**, *135*, 10274–10277. [[CrossRef](#)] [[PubMed](#)]
16. Mahler, B.; Hoepfner, V.; Liao, K.; Ozin, G.A. Colloidal synthesis of 1T-WS₂ and 2H-WS₂ nanosheets: Applications for photocatalytic hydrogen evolution. *J. Am. Chem. Soc.* **2014**, *136*, 14121–14127. [[CrossRef](#)]
17. Li, H.; Wu, J.; Yin, Z.; Zhang, H. Preparation and applications of mechanically exfoliated single-layer and multilayer MoS(2) and WSe(2) nanosheets. *Acc. Chem. Res.* **2014**, *47*, 1067–1075. [[CrossRef](#)]
18. Shi, Y.; Wang, J.; Wang, C.; Zhai, T.T.; Bao, W.J.; Xu, J.J.; Xia, X.H.; Chen, H.Y. Hot electron of Au nanorods activates the electrocatalysis of hydrogen evolution on MoS₂ nanosheets. *J. Am. Chem. Soc.* **2015**, *137*, 7365–7370. [[CrossRef](#)]
19. Gao, S.; Lin, Y.; Jiao, X.; Sun, Y.; Luo, Q.; Zhang, W.; Li, D.; Yang, J.; Xie, Y. Partially oxidized atomic cobalt layers for carbon dioxide electroreduction to liquid fuel. *Nature* **2016**, *529*, 68–71. [[CrossRef](#)]
20. Shin, S.; Jin, Z.; Kwon, D.H.; Bose, R.; Min, Y.S. High turnover frequency of hydrogen evolution reaction on amorphous MoS₂ thin film directly grown by atomic layer deposition. *Langmuir ACS J. Surf. Colloids* **2015**, *31*, 1196–1202. [[CrossRef](#)]
21. Liu, W.; Liu, H.; Dang, L.; Zhang, H.; Wu, X.; Yang, B.; Li, Z.; Zhang, X.; Lei, L.; Jin, S. Amorphous cobalt-iron hydroxide nanosheet electrocatalyst for efficient electrochemical and photo-electrochemical oxygen evolution. *Adv. Funct. Mater.* **2017**, *27*, 1603904. [[CrossRef](#)]
22. Yang, L.; Guo, Z.; Huang, J.; Xi, Y.; Gao, R.; Su, G.; Wang, W.; Cao, L.; Dong, B. Vertical growth of 2D amorphous FePO₄ nanosheet on ni foam: Outer and inner structural design for superior water splitting. *Adv. Mater.* **2017**, *29*, 4574. [[CrossRef](#)] [[PubMed](#)]
23. Li, C.; Mei, X.; Lam, F.L.-Y.; Hu, X. Amorphous iron and cobalt based phosphate nanosheets supported on nickel foam as superior catalysts for hydrogen evolution reaction. *ACS Appl. Energy Mater.* **2018**, *1*, 6764–6768. [[CrossRef](#)]
24. He, J.; Qian, T.; Cai, C.; Xiang, X.; Li, S.; Zu, X. Nickel-based selenides with a fractal structure as an excellent bifunctional electrocatalyst for water splitting. *Nanomaterials* **2022**, *12*, 281. [[CrossRef](#)]
25. Cai, C.; Han, S.B.; Zhang, X.T.; Yu, J.X.; Xiang, X.; Yang, J.; Qiao, L.; Zu, X.T.; Chen, Y.Z.; Li, S.A. Ultrahigh oxygen evolution reaction activity in Au doped co-based nanosheets. *RSC Adv.* **2022**, *12*, 6205–6213. [[CrossRef](#)]
26. Cai, C.; Liu, K.; Zhu, Y.; Li, P.; Wang, Q.; Liu, B.; Chen, S.; Li, H.; Zhu, L.; Li, H.; et al. Optimizing hydrogen binding on Ru sites with RuCo alloy nanosheets for efficient alkaline hydrogen evolution. *Angew. Chem.* **2022**, *134*, e202113664. [[CrossRef](#)]
27. Jiang, D.L.; Xu, Y.; Yang, R.; Li, D.; Meng, S.C.; Chen, M. CoP₃/CoMoP Heterogeneous nanosheet arrays as robust electrocatalyst for pH-universal hydrogen evolution reaction. *ACS Sustain. Chem. Eng.* **2019**, *7*, 9309–9317. [[CrossRef](#)]
28. Cai, C.; Han, S.; Wang, Q.; Gu, M. Direct observation of yolk-shell transforming to gold single atoms and clusters with superior oxygen evolution reaction efficiency. *ACS Nano* **2019**, *13*, 8865–8871. [[CrossRef](#)]
29. Huang, J.; Chen, J.; Yao, T.; He, J.; Jiang, S.; Sun, Z.; Liu, Q.; Cheng, W.; Hu, F.; Jiang, Y.; et al. CoOOH Nanosheets with High Mass Activity for Water Oxidation. *Angew. Chem.* **2015**, *54*, 8722–8727. [[CrossRef](#)]

30. Kwak, I.H.; Im, H.S.; Jang, D.M.; Kim, Y.W.; Park, K.; Lim, Y.R.; Cha, E.H.; Park, J. CoSe(2) and NiSe(2) Nanocrystals as Superior Bifunctional Catalysts for Electrochemical and Photoelectrochemical Water Splitting. *ACS Appl. Mater. Interfaces* **2016**, *8*, 5327–5334. [[CrossRef](#)]
31. Zhuang, Z.; Sheng, W.; Yan, Y. Synthesis of Monodisperse Au@Co₃O₄ Core-Shell Nanocrystals and Their Enhanced Catalytic Activity for Oxygen Evolution Reaction. *Adv. Mater.* **2014**, *26*, 3950–3955. [[CrossRef](#)] [[PubMed](#)]
32. Yin, J.; Li, Y.; Lv, F.; Fan, Q.; Zhao, Y.-Q.; Zhang, Q.; Wang, W.; Cheng, F.; Xi, P.; Guo, S. NiO/CoN Porous Nanowires as Efficient Bifunctional Catalysts for Zn-Air Batteries. *ACS Nano* **2017**, *11*, 2275–2283. [[CrossRef](#)] [[PubMed](#)]
33. Gao, M.R.; Cao, X.; Gao, Q.; Xu, Y.F.; Zheng, Y.R.; Jiang, J.; Yu, S.H. Nitrogen-doped graphene supported CoSe(2) nanobelt composite catalyst for efficient water oxidation. *ACS Nano* **2014**, *8*, 3970–3978. [[CrossRef](#)]
34. Liu, Y.; Jin, Z.; Li, P.; Tian, X.; Chen, X.; Xiao, D. Boron- and Iron-Incorporated α -Co(OH)₂ Ultrathin Nanosheets as an Efficient Oxygen Evolution Catalyst. *ChemElectroChem* **2018**, *5*, 593–597. [[CrossRef](#)]
35. Xiao, X.; He, C.-T.; Zhao, S.; Li, J.; Lin, W.; Yuan, Z.; Zhang, Q.; Wang, S.; Dai, L.; Yu, D. A general approach to cobalt-based homobimetallic phosphide ultrathin nanosheets for highly efficient oxygen evolution in alkaline media. *Energy Environ. Sci.* **2017**, *10*, 893–899. [[CrossRef](#)]
36. Li, J.; Zhou, Q.; Zhong, C.; Li, S.; Shen, Z.; Pu, J.; Liu, J.; Zhou, Y.; Zhang, H.; Ma, H. (Co/Fe)₄O₄ Cubane-Containing Nanorings Fabricated by Phosphorylating Cobalt Ferrite for Highly Efficient Oxygen Evolution Reaction. *ACS Catal.* **2019**, *9*, 3878–3887. [[CrossRef](#)]
37. Li, G.L.; Zhang, X.B.; Zhang, H.; Liao, C.Y.; Jiang, G.B. Bottom-up MOF-intermediated synthesis of 3D hierarchical flower-like cobalt-based homobimetallic phosphide composed of ultrathin nanosheets for highly efficient oxygen evolution reaction. *Appl. Catal. B-Environ.* **2019**, *249*, 147–154. [[CrossRef](#)]
38. Tan, P.; Wu, Z.; Chen, B.; Xu, H.R.; Cai, W.Z.; Ni, M. Exploring oxygen electrocatalytic activity and pseudocapacitive behavior of Co₃O₄ nanoplates in alkaline solutions. *Electrochim. Acta* **2019**, *310*, 86–95. [[CrossRef](#)]
39. Babu, D.D.; Huang, Y.; Anandhababu, G.; Wang, X.; Si, R.; Wu, M.; Li, Q.; Wang, Y.; Yao, J. Atomic iridium@cobalt nanosheets for dinuclear tandem water oxidation. *J. Mater. Chem. A* **2019**, *7*, 8376–8383. [[CrossRef](#)]
40. Ouyang, T.; Ye, Y.Q.; Wu, C.Y.; Xiao, K.; Liu, Z.Q. Heterostructures Composed of N-Doped Carbon Nanotubes Encapsulating Cobalt and beta-Mo₂C Nanoparticles as Bifunctional Electrodes for Water Splitting. *Angew. Chem.* **2019**, *58*, 4923–4928. [[CrossRef](#)] [[PubMed](#)]
41. Pei, Y.; Guo, P.; Qiao, M.; Li, H.; Wei, S.; He, H.; Fan, K. The modification effect of Fe on amorphous CoB alloy catalyst for chemoselective hydrogenation of crotonaldehyde. *J. Catal.* **2007**, *248*, 303–310. [[CrossRef](#)]
42. Shi, Y.; Luo, H.Q.; Li, N.B. Determination of the critical premicelle concentration, first critical micelle concentration and second critical micelle concentration of surfactants by resonance Rayleigh scattering method without any probe. *Spectrochim. Acta. Part A Mol. Biomol. Spectrosc.* **2011**, *78*, 1403–1407. [[CrossRef](#)]
43. Zhou, D.; Wang, S.; Jia, Y.; Xiong, X.; Yang, H.; Liu, S.; Tang, J.; Zhang, J.; Liu, D.; Zheng, L.; et al. NiFe hydroxide lattice tensile strain: Enhancement of adsorption of oxygenated intermediates for efficient water oxidation catalysis. *Angew. Chem.* **2019**, *58*, 736–740. [[CrossRef](#)]
44. Strickler, A.L.; Escudero-Escribano, M.A.; Jaramillo, T.F. Core-shell Au@Metal-Oxide nanoparticle electrocatalysts for enhanced oxygen evolution. *Nano Lett.* **2017**, *17*, 6040–6046. [[CrossRef](#)]
45. Zhang, H.; Zhang, J.; Li, Y.; Jiang, H.; Jiang, H.; Li, C. Continuous oxygen vacancy engineering of the Co₃O₄ layer for an enhanced alkaline electrocatalytic hydrogen evolution reaction. *J. Mater. Chem. A* **2019**, *7*, 13506–13510. [[CrossRef](#)]
46. Zhou, Y.; Wang, Z.; Pan, Z.; Liu, L.; Xi, J.; Luo, X.; Shen, Y. Exceptional performance of hierarchical Ni-Fe (hydr)oxide@NiCu electrocatalysts for water splitting. *Adv. Mater.* **2019**, *31*, e1806769. [[CrossRef](#)]
47. Kim, B.J.; Fabbri, E.; Abbott, D.F.; Cheng, X.; Clark, A.H.; Nachttegaal, M.; Borlaf, M.; Castelli, I.E.; Graule, T.; Schmidt, T.J. Functional role of Fe-doping in Co-based perovskite oxide catalysts for oxygen evolution reaction. *J. Am. Chem. Soc.* **2019**, *141*, 5231–5240. [[CrossRef](#)]
48. Zhuang, L.; Ge, L.; Yang, Y.; Li, M.; Jia, Y.; Yao, X.; Zhu, Z. Ultrathin iron-cobalt oxide nanosheets with abundant oxygen vacancies for the oxygen evolution reaction. *Adv. Mater.* **2017**, *29*, 6793. [[CrossRef](#)]
49. Xu, L.; Jiang, Q.; Xiao, Z.; Li, X.; Huo, J.; Wang, S.; Dai, L. Plasma-engraved Co₃O₄ nanosheets with oxygen vacancies and high surface area for the oxygen evolution reaction. *Angew. Chem.* **2016**, *55*, 5277–5281. [[CrossRef](#)]
50. Kwon, G.; Jang, H.; Lee, J.S.; Mane, A.; Mandia, D.J.; Soltau, S.R.; Utschig, L.M.; Martinson, A.B.F.; Tiede, D.M.; Kim, H.; et al. Resolution of electronic and structural factors underlying oxygen-evolving performance in amorphous cobalt oxide catalysts. *J. Am. Chem. Soc.* **2018**, *140*, 10710–10720. [[CrossRef](#)]
51. Li, X.; Sun, Y.; Wu, Q.; Liu, H.; Gu, W.; Wang, X.; Cheng, Z.; Fu, Z.; Lu, Y. Optimized electronic configuration to improve the surface absorption and bulk conductivity for enhanced oxygen evolution reaction. *J. Am. Chem. Soc.* **2019**, *141*, 3121–3128. [[CrossRef](#)]
52. Song, F.; Bai, L.; Moysiadou, A.; Lee, S.; Hu, C.; Liardet, L.; Hu, X. Transition metal oxides as electrocatalysts for the oxygen evolution reaction in alkaline solutions: An application-inspired renaissance. *J. Am. Chem. Soc.* **2018**, *140*, 7748–7759. [[CrossRef](#)]
53. Grimaud, A.; Diaz-Morales, O.; Han, B.; Hong, W.T.; Lee, Y.-L.; Giordano, L.; Stoerzinger, K.A.; Koper, M.T.M.; Shao-Horn, Y. Activating lattice oxygen redox reactions in metal oxides to catalyze oxygen evolution. *Nat. Chem.* **2017**, *9*, 457–465. [[CrossRef](#)]
54. Han, X.T.; Yu, C.; Zhou, S.; Zhao, C.T.; Huang, H.W.; Yang, J.; Liu, Z.B.; Zhao, J.J.; Qiu, J.S. Ultrasensitive iron-triggered nanosized Fe-CoOOH integrated with graphene for highly efficient oxygen evolution. *Adv. Energy Mater.* **2017**, *7*, 1602148. [[CrossRef](#)]

55. Trang-Thi Hong, N.; Lee, J.; Bae, J.; Lim, B. Binary FeCo oxyhydroxide nanosheets as highly efficient bifunctional electrocatalysts for overall water splitting. *Chem. A Eur. J.* **2018**, *24*, 4724–4728.
56. Zhou, H.; Yu, F.; Sun, J.; He, R.; Chen, S.; Chu, C.W.; Ren, Z. Highly active catalyst derived from a 3D foam of $\text{Fe}(\text{PO}_3)_2/\text{Ni}_2\text{P}$ for extremely efficient water oxidation. *Proc. Natl. Acad. Sci. USA* **2017**, *114*, 5607–5611. [[CrossRef](#)]
57. Chen, J.; Zheng, F.; Zhang, S.-J.; Fisher, A.; Zhou, Y.; Wang, Z.; Li, Y.; Xu, B.-B.; Li, J.-T.; Sun, S.-G. Interfacial interaction between FeOOH and Ni–Fe LDH to modulate the local electronic structure for enhanced OER electrocatalysis. *ACS Catal.* **2018**, *8*, 11342–11351. [[CrossRef](#)]
58. Vile, G.; Bildstein, R.S.; Lhuillery, A.; Rueedi, G. Electrophile, substrate functionality, and catalyst effects in the synthesis of α -mono and di-substituted benzylamines via visible-light photoredox catalysis in flow. *ChemCatChem* **2018**, *10*, 3786–3794. [[CrossRef](#)]
59. Sivo, A.; Galaverna, R.D.; Gomes, G.R.; Pastre, J.C.; Vile, G. From circular synthesis to material manufacturing: Advances, challenges, and future steps for using flow chemistry in novel application area. *React. Chem. Eng.* **2021**, *6*, 756–786. [[CrossRef](#)]